Transient and steady convection in two dimensions

Ambrish Pandey[1,2] and **Katepalli R. Sreenivasan**[2,3]

[1]Department of Physics, Indian Institute of Technology Roorkee, Roorkee 247667, Uttarakhand, India

[2]Center for Astrophysics and Space Science, New York University Abu Dhabi, Abu Dhabi 129188, United Arab Emirates

[3]Tandon School of Engineering, Department of Physics, and Courant Institute of Mathematical Sciences, New York University, New York, NY 11201, USA

Corresponding author: Katepalli R. Sreenivasan, katepalli.sreenivasan@nyu.edu

We simulate thermal convection in a two-dimensional square box using the no-slip condition on all boundaries, and isothermal bottom and top walls, and adiabatic sidewalls. We choose 0.1 and 1 for the Prandtl number Pr and vary the Rayleigh number Ra between 10^6 and 10^{12}. We particularly study the temporal evolution of integral transport quantities towards their steady states. Perhaps not surprisingly, the velocity field evolves more slowly than the thermal field, and its steady state – which is nominal in the sense that large-amplitude low-frequency oscillations persist around plausible averages – is reached exponentially. We study these oscillation characteristics. The transient time for the velocity field to achieve its nominal steady state increases almost linearly with the Reynolds number. For large Ra, the Reynolds number itself scales almost as $Ra^{2/3} \, Pr^{-1}$, and the Nusselt number as $Ra^{2/7}$.

Key words: turbulent convection, turbulence simulation, Bénard convection

1. Introduction

Turbulent flows driven by buoyancy due to inhomogeneity of the temperature are common in nature and applications (Verma 2018; Schumacher & Sreenivasan 2020; Lohse & Shishkina 2023). Rayleigh–Bénard convection (RBC) is a paradigm for such flows. The RBC originally referred to shallow horizontally extended layers of fluid, heated from below and cooled from above, and the horizontal walls are smooth unless otherwise specified. In this traditional paradigm, RBC is entirely governed by Prandtl and Rayleigh

numbers – where the Prandtl number Pr is the ratio of the kinematic viscosity ν to the thermal diffusivity κ of the fluid, and the Rayleigh number Ra is the ratio of the forcing strength to the dissipative mechanisms. Heat and momentum transport across the convective fluid layer are two global responses to thermal driving in RBC. Heat transport is measured by the Nusselt number Nu, which is the total heat flux relative to that by conduction in the absence of fluid motion, and the momentum transport by an appropriate Reynolds number Re, which defines the flow strength.

Because the Rayleigh number is proportional to H^3, where H is the height of the convection apparatus, there has been a tendency in the last 25 or so years to choose as high a value of H as possible while, by necessity, shrinking the horizontal dimension (e.g. Castaing *et al.* 1989; Niemela *et al.* 2000). The same is also true of direct numerical simulations (DNS) (e.g. Stevens, Lohse & Verzicco 2011; Iyer *et al.* 2020). The choice of a low aspect ratio $\Gamma \equiv L/H$ (where L is the horizontal dimension of the apparatus) is common in the quest to achieve very high Rayleigh numbers, but an organised motion that develops in such flows has its own structural morphology (Kadanoff 2001; Sreenivasan, Bershadskii & Niemela 2002; Chillà & Schumacher 2012; Foroozani *et al.* 2014, 2017; Verma, Kumar & Pandey 2017) that depends on the aspect ratio and the shape of the apparatus; see also Pandey *et al.* (2022a) and Stevens *et al.* (2024). Pure scaling laws in such flows are unlikely for all conditions, yet it is common to fit the Nusselt and Reynolds numbers by power laws with respect to Ra, i.e $Nu \sim Ra^\gamma$ and $Re \sim Ra^\zeta$. As pointed out by Doering (2020), fitting such local exponents for small ranges of data is bound to lead to conclusions of uncertain value. Indeed, there are considerable variations of the effective exponents γ and ζ from one study to another, and they have been the subject of extensive reviews – e.g. by Chillà & Schumacher (2012) and Lohse & Shishkina (2024). In a series of large simulations, an effort has been made to avoid the constraining effect of the sidewalls by stipulating periodic boundary conditions on them (Samuel *et al.* 2024). These studies mimicking large aspect ratio convection have revealed a very different nature of near-wall velocity from a traditional boundary layer that undergoes laminar–turbulent transition, and have implications for the so-called ultimate state.

There has been the expectation that the riddle of the ultimate state can be solved for the two-dimensional (2-D) case in which the flow is compelled to occur only in a vertical plane (Zhu *et al.* 2018; Samuel & Verma 2024; Tiwari, Sharma & Verma 2025) because of the natural hope that very high Rayleigh numbers can be achieved here for the same computing power. Existing data show a heat transport scaling that is similar to the three-dimensional (3-D) counterpart (Schmalzl, Breuer & Hansen 2004; van der Poel, Stevens & Lohse 2013; Pandey *et al.* 2016; Zhang, Zhou & Sun 2017; Pandey 2021) but the Nusselt number in two dimensions is smaller when $Pr \geqslant 1$ (van der Poel *et al.* 2013), although essentially the same when Pr is small (Pandey 2021), as for liquid metals. The Reynolds number, on the other hand, shows very different behaviours in two and three dimensions. The magnitudes of momentum transport and the scaling exponent ζ are consistently higher in two dimensions, with $\zeta \geqslant 0.60$ (Schmalzl *et al.* 2004; van der Poel *et al.* 2013; Zhang *et al.* 2017; Wan *et al.* 2020; Pandey 2021). As a summary, the exponent γ has been reported to take values in the range $[1/4, 1/3]$, while ζ assumes values in the range $[4/9, 2/3]$ (Verma 2018). Note that these scaling features are well captured by the model of Grossmann & Lohse (2000); see also Pandey *et al.* (2016).

In this paper, we perform DNS of 2-D convection in a unit box for $Pr = 0.1$ and 1, for Rayleigh numbers between 10^6 and 10^{12}, not only for the purposes of exploring flow properties, but also for highlighting the challenges of simulating 2-D convection. We use the no-slip condition on all boundaries, with bottom and top walls isothermal, and sidewalls adiabatic. In particular, we show that the velocity field evolves more slowly

than the temperature, and call attention to large fluctuations that occur in what may be regarded as the nominal steady state of the velocity field; it is nominal in the sense that large-amplitude low-frequency oscillations persist around plausible averages. (To avoid excessive repetition, however, we often omit the qualifier 'nominal'.) We relate these fluctuations to heat transport characteristics, and provide estimates of suitably defined transient times. Heat transport also exhibits persistently wild fluctuations about its mean for strong thermal forcing. The main qualitative conclusion of this study is that such long transients, as well as wildly fluctuating heat transport, at least for aspect ratios of order unity, make the observation of the so-called ultimate state as elusive in two dimensions (Doering, Toppaladoddi & Wettlaufer 2019) as in three dimensions (Doering 2020).

2. Numerical methodology

We perform DNS in a 2-D fluid layer with horizontal dimension L, with an imposed temperature difference ΔT between the bottom and top plates separated by vertical dimension H. For this work, the aspect ratio is $\Gamma = L/H = 1$. The following Oberbeck–Boussinesq equations dictating the flow are solved using the Nek5000 solver (which has been used extensively for the simulation of turbulent convection – for details, see Scheel, Emran & Schumacher 2013):

$$\nabla \cdot \boldsymbol{u} = 0, \tag{2.1}$$

$$\frac{\partial \boldsymbol{u}}{\partial t} + \boldsymbol{u} \cdot \nabla \boldsymbol{u} = -\frac{\nabla p}{\rho_0} + \alpha g (T - T_0)\hat{z} + \nu \nabla^2 \boldsymbol{u}, \tag{2.2}$$

$$\frac{\partial T}{\partial t} + \boldsymbol{u} \cdot \nabla T = \kappa \nabla^2 T. \tag{2.3}$$

Here, $\boldsymbol{u} = (u_x, u_z)$, p and T are the velocity, pressure and temperature, respectively; ρ_0 is the reference density, and T_0 is the reference temperature. We non-dimensionalise (2.1)–(2.3) using H, ΔT, u_f and t_f as the scales for length, temperature, velocity and time, respectively, where $u_f = \sqrt{\alpha g\, \Delta TH}$ is the free-fall velocity, and $t_f = H/u_f$ is the free-fall time. The result contains the Prandtl number Pr and the Rayleigh number $Ra = \alpha g\, \Delta TH^3/(\nu\kappa)$, where α is the isobaric thermal expansion coefficient, and g is the acceleration due to gravity. We explore two fluids with $Pr = 0.1$ and 1 for Ra between 10^6 and 10^{12}. The square domain is decomposed into N_e elements, and each element is further resolved using Lagrangian interpolation polynomials of order N in both horizontal and vertical directions. Thus the entire flow is resolved using $N_e N^2$ mesh cells. The no-slip condition for the velocity field is imposed on all boundaries. Isothermal and adiabatic conditions for the temperature field are imposed on the horizontal plates and sidewalls, respectively. The flow consists of a single large-scale structure covering the entire domain, except for $Pr = 1$, $Ra \leqslant 10^7$, where two vertically stacked structures occur. The flow morphology is similar to that observed by Labarre, Fauve & Chibbaro (2023) and Samuel & Verma (2024), so we do not show it here.

To resolve the thermal and viscous boundary layers, finer mesh is used near all boundaries. The spatial resolution in the flow is further ensured by computing the Kolmogorov length scale η, which is nominally the finest scale in the velocity field, and stipulating that the local vertical grid spacing is $\Delta_z(z)/\eta(z) < 1.5$ for all simulations. The kinetic energy and the thermal dissipation rates are defined, respectively, as

$$\varepsilon_u(\boldsymbol{x}) = \frac{\nu}{2} \sum_{l,m} \left(\frac{\partial u_l}{\partial x_m} + \frac{\partial u_m}{\partial x_l} \right)^2, \tag{2.4}$$

$$\varepsilon_T(\boldsymbol{x}) = \kappa \left(\frac{\partial T}{\partial x_l}\right)^2, \tag{2.5}$$

and represent the rates of loss of kinetic energy and thermal energy per unit mass. Here, l, $m = (x, z)$, and the local Kolmogorov scale is given by $\eta = (\nu^3/\varepsilon_u)^{1/4}$. As the intermittent variation of $\varepsilon_u(\boldsymbol{x})$ in the flow leads to variations in the Kolmogorov scale as well, we estimate an average Kolmogorov scale in each horizontal plane using the horizontally and temporally averaged dissipation as

$$\eta(z) = \frac{\nu^{3/4}}{\langle \varepsilon_u \rangle_{x,t}^{1/4}(z)}. \tag{2.6}$$

The finest length scale in the temperature field, the Batchelor scale $\eta/\sqrt{Pr}$, is of the same order as η, or coarser, in the present work. Thus it is always adequately resolved.

3. Other associated definitions

The Nusselt number in a horizontal plane is computed as (Chillà & Schumacher 2012)

$$Nu(z) = \frac{\langle u_z T \rangle_{x,t} - \kappa \partial \langle T \rangle_{x,t}/\partial z}{\kappa \Delta T/H}, \tag{3.1}$$

where $\langle u_z T \rangle_{x,t}$ is the convective component of the heat flux, and $-\kappa \partial \langle T \rangle_{x,t}/\partial z$ is the diffusive component. As the vertical velocity vanishes at the horizontal plates, this relation yields the definition using the wall temperature gradient as

$$Nu_W = -\frac{H}{\Delta T} \left.\frac{\partial \langle T \rangle_{x,t}}{\partial z}\right|_{z=0,H}. \tag{3.2}$$

Averaging (3.1) along the vertical direction yields the following relation for the global heat transport across the convective layer:

$$Nu = 1 + \frac{H}{\kappa \Delta T} \langle u_z T \rangle_{A,t}. \tag{3.3}$$

Here, $\langle \cdot \rangle_{A,t}$ stands for the average over the entire flow domain and simulation time covering the steady state.

In another family of relations, the exact relations in RBC (Howard 1972; Shraiman & Siggia 1990) connect the Nusselt number Nu with the globally averaged kinetic energy dissipation rate ε_u and the thermal dissipation rate ε_T, as

$$\langle \varepsilon_u \rangle_{A,t} = \frac{\nu^3}{H^4} \frac{(Nu-1)Ra}{Pr^2}, \tag{3.4}$$

$$\langle \varepsilon_T \rangle_{A,t} = \kappa \frac{(\Delta T)^2}{H^2} Nu. \tag{3.5}$$

Thus the Nusselt number can also be estimated from mean dissipation rates:

$$Nu_{\varepsilon_u} = 1 + \frac{H^4}{\nu^3} \frac{Pr^2}{Ra} \langle \varepsilon_u \rangle_{A,t}, \tag{3.6}$$

$$Nu_{\varepsilon_T} = \frac{H^2}{(\Delta T)^2} \frac{\langle \varepsilon_T \rangle_{A,t}}{\kappa}. \tag{3.7}$$

The agreement among simulated values from different definitions serves as a check on the accuracy and adequacy of spatial and temporal resolutions

1015 A42-4

Pr	Ra	$N_e N^2$	Nu	Nu_{ε_u}	Nu_{ε_T}	Nu_W	Re	$t_{sim}(t_f)$
0.1	10^6	690^2	5.91 ± 0.1	5.91 ± 0.4	5.91 ± 0.4	5.91 ± 0.5	1916 ± 96	605
0.1	2×10^6	300^2	7.05 ± 0.1	7.05 ± 0.1	7.05 ± 0.1	7.05 ± 0.9	2747 ± 18	1159
0.1	3×10^6	300^2	7.88 ± 0.1	7.88 ± 0.1	7.88 ± 0.1	7.88 ± 1.2	3396 ± 27	1184
0.1	6×10^6	300^2	10.04 ± 0.7	9.97 ± 0.6	9.97 ± 1.2	9.98 ± 1.6	4979 ± 428	2684
0.1	10^7	690^2	11.77 ± 1.1	11.78 ± 0.9	11.75 ± 1.3	11.73 ± 1.7	6521 ± 514	2152
0.1	2×10^7	500^2	15.35 ± 2.1	15.32 ± 1.1	15.29 ± 1.5	15.30 ± 1.9	9512 ± 968	3007
0.1	3×10^7	690^2	17.50 ± 8.6	17.52 ± 3.2	17.52 ± 2.5	17.48 ± 3.0	$12\,065 \pm 2981$	1415
0.1	10^8	1150^2	23.01 ± 12	22.97 ± 4.3	23.05 ± 3.0	23.06 ± 3.7	$22\,316 \pm 5024$	1081
0.1	3×10^8	1150^2	31.06 ± 16	30.82 ± 7.2	30.75 ± 3.7	30.76 ± 4.7	$43\,375 \pm 9299$	1116
0.1	10^9	2070^2	42.72 ± 24	42.28 ± 12	42.70 ± 4.9	42.72 ± 6.5	$95\,499 \pm 15\,598$	304
0.1	3×10^9	2230^2	59.15 ± 41	58.71 ± 14	59.04 ± 6.2	58.99 ± 7.8	$2\,00\,001 \pm 22\,805$	222
0.1	10^{10}	3122^2	84.74 ± 58	79.24 ± 26	84.94 ± 8.6	84.91 ± 12	$4\,46\,638 \pm 56\,213$	178
1	3×10^6	300^2	6.01 ± 0.3	6.01 ± 0.1	6.01 ± 0.1	6.01 ± 0.6	289 ± 33	6375
1	6×10^6	300^2	7.11 ± 0.1	7.11 ± 0.1	7.11 ± 0.1	7.11 ± 0.3	423 ± 4	6623
1	8×10^6	300^2	8.18 ± 0.1	8.18 ± 0.1	8.18 ± 0.2	8.18 ± 0.7	530 ± 21	3630
1	9×10^6	300^2	8.64 ± 0.2	8.64 ± 0.1	8.65 ± 0.2	8.65 ± 0.8	580 ± 21	5512
1	10^7	300^2	9.03 ± 0.2	9.03 ± 0.1	9.03 ± 0.2	9.03 ± 1.0	626 ± 25	5188
1	1.5×10^7	300^2	13.33 ± 1.2	13.35 ± 0.7	13.34 ± 1.2	13.33 ± 1.7	918 ± 129	7056
1	2×10^7	690^2	14.75 ± 4.5	14.74 ± 1.2	14.83 ± 1.7	14.79 ± 1.8	1108 ± 366	1879
1	3×10^7	690^2	17.27 ± 3.4	17.00 ± 1.4	16.98 ± 1.9	17.10 ± 2.1	1376 ± 337	2782
1	6×10^7	690^2	21.48 ± 4.8	21.57 ± 1.8	21.57 ± 2.3	21.56 ± 2.4	2010 ± 442	2584
1	10^8	690^2	25.01 ± 5.6	25.20 ± 2.0	25.22 ± 2.5	25.21 ± 2.3	2665 ± 432	1717
1	3×10^8	690^2	35.61 ± 7.5	35.85 ± 1.8	35.84 ± 2.2	35.88 ± 2.0	4936 ± 627	2379
1	6×10^8	690^2	44.15 ± 12	44.01 ± 2.3	44.04 ± 2.2	44.02 ± 2.2	7385 ± 954	1178
1	10^9	700^2	50.87 ± 35	51.14 ± 10	51.29 ± 5.0	51.20 ± 6.3	$12\,012 \pm 3324$	2112
1	3×10^9	1150^2	67.15 ± 43	68.32 ± 12	68.17 ± 6.3	68.26 ± 8.4	$20\,958 \pm 5152$	1479
1	10^{10}	1150^2	94.52 ± 57	94.93 ± 21	95.26 ± 8.5	94.97 ± 12	$43\,533 \pm 8819$	989
1	3×10^{10}	1610^2	130.2 ± 84	129.7 ± 34	130.3 ± 12	130.3 ± 18	$89\,031 \pm 18\,989$	1105
1	10^{11}	2070^2	183.3 ± 128	184.1 ± 56	185.2 ± 17	184.7 ± 23	$1\,99\,858 \pm 41\,998$	1268
1	3×10^{11}	3122^2	262.3 ± 185	260.7 ± 109	262.2 ± 24	262.1 ± 36	$3\,95\,763 \pm 69\,299$	336
1	10^{12}	5210^2	394.2 ± 286	376.1 ± 88	395.8 ± 36	395.3 ± 54	$10\,85\,094 \pm 54\,592$	253

Table 1. Important parameters of DNS in a 2-D box with $\Gamma = 1$. We list the Prandtl number, the Rayleigh number, the total number of mesh cells in the entire flow domain $N_e N^2$, the Nusselt numbers using (3.3), (3.6), (3.7) and (3.2), respectively, the Reynolds number, and the simulation time after the flow attains a steady state, t_{sim}. Error bars in Nusselt and Reynolds numbers are the corresponding standard deviations.

(Stevens, Verzicco & Lohse 2010; Zhang *et al.* 2017; Pandey *et al.* 2022*a*). In table 1, we list the global heat flux estimated from all the methods, and note that the agreement among various estimates of the Nusselt number is indeed very good. Also listed are other crucial parameters of the flow. We discuss below the approach to the final state of the Nusselt number using these definitions and relations, with comments on the scaling of global averages. In (3.1)–(3.3) and (3.6)–(3.7), the Nusselt numbers are globally averaged quantities, though we do not show the averaging symbol explicitly, following standard usage of the past.

In the following, we study the evolutions of the instantaneous domain-averaged heat fluxes, which are defined as

$$\overline{Nu} = 1 + \frac{H}{\kappa \Delta T} \langle u_z T \rangle_A, \tag{3.8}$$

$$\overline{Nu_{\varepsilon_u}} = 1 + \frac{H^4}{\nu^3} \frac{Pr^2}{Ra} \langle \varepsilon_u \rangle_A, \tag{3.9}$$
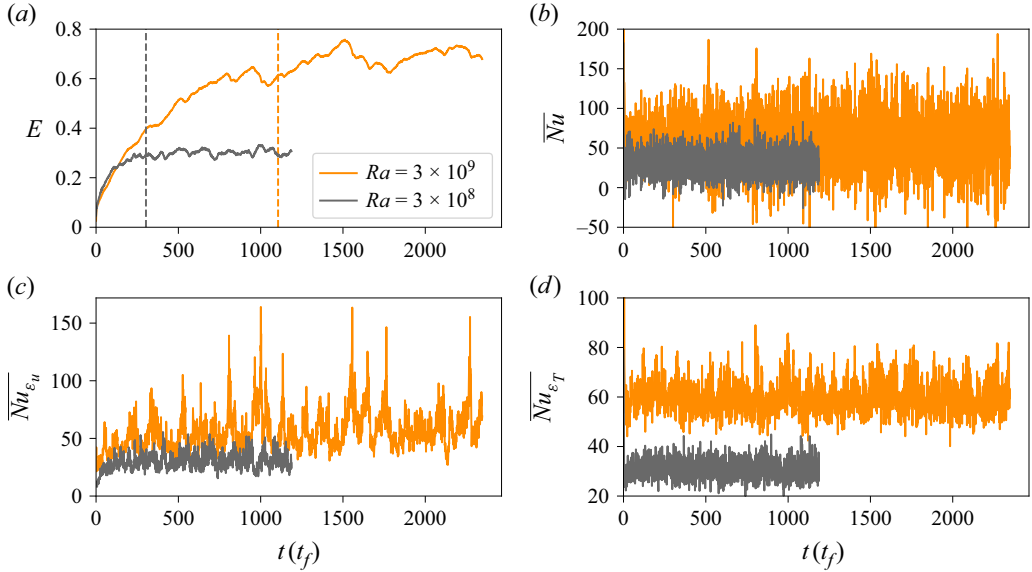
Figure 1. Evolution of the integral quantities in the transient state for $Pr = 0.1$, and $Ra = 3 \times 10^8$ (black curves) and $Ra = 3 \times 10^9$ (orange curves). (a) The domain-averaged kinetic energy E increases slowly and takes a few thousand free-fall times to reach the steady state. The transient time is longer for higher Ra. Dashed vertical lines show a quantitative measure of the transient time t_{trns}, obtained from (4.3), to be discussed later. (b,c,d) Plots show that the Nusselt number fluctuates rapidly about its mean nearly from the start, but fluctuations have different characters depending on the definition of the Nusselt number. In (b), the fluctuations in $\overline{Nu}$ are strong and of high frequency with no well-defined transient state, and there is an overlap for the two Ra values. In (c), one can approximately identify a transient state in $\overline{Nu_{\varepsilon_u}}$, which exhibits very strong fluctuations containing both high and low frequencies. Plot (d) shows that $\overline{Nu_{\varepsilon_T}}$ fluctuates similarly to $\overline{Nu}$ in (b), but there is no overlap for the two Rayleigh numbers. The occasional appearance of negative values of $\overline{Nu}$ suggests the likelihood that a small parcel of the coldest fluid from the top wall registers directly at the bottom wall, and vice versa.

$$\overline{Nu_{\varepsilon_T}} = \frac{H^2}{(\Delta T)^2} \frac{\langle \varepsilon_T \rangle_A}{\kappa}. \tag{3.10}$$

4. Transient characteristics

A common method for initiating high-Ra simulations is to start them from the flow at a lower Ra value. Simulations can also be performed *ab initio* from the conduction state with random perturbations. In both cases, global heat flux and kinetic energy evolve with time, and one needs to wait some time before a statistically steady state is attained. Figure 1 shows the temporal evolution of integral quantities for the two Ra indicated and $Pr = 0.1$, with simulations initiated from the conduction state. On the one hand, we observe that $\overline{Nu}$ and $\overline{Nu_{\varepsilon_T}}$ in figure 1(b,d) start oscillating about some mean value shortly after the simulation begins. On the other hand, $\overline{Nu_{\varepsilon_u}}$ in figure 1(c) initially increases and starts to fluctuate about a mean value only after some time has elapsed. The instantaneous domain-averaged non-dimensional kinetic energy $E = \langle (u_x^2 + u_z^2)/2 \rangle_A / u_f^2$ in figure 1(a) offers the best means to determine the time to the steady state. There is no ambiguity about this approach for the lower Ra; however, aside from the fact that it takes longer at the higher Ra for the energy to achieve its steady state, the latter is somewhat nominal because fluctuations about the average are significant. The situation becomes more so at
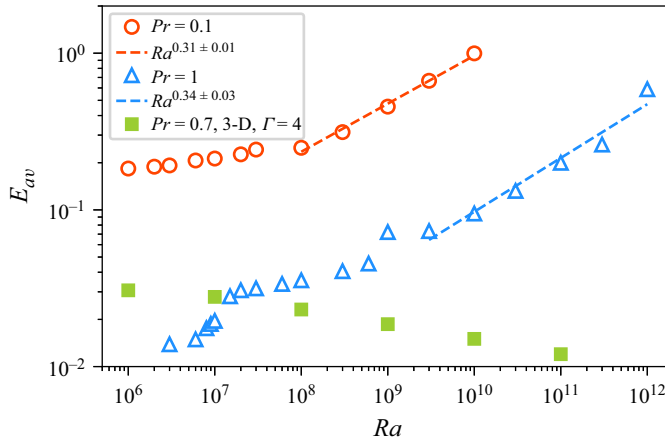
Figure 2. Global (area- as well as time-averaged) kinetic energy in the steady state E_{av} as a function of Ra. An increasing trend with Ra is observed in 2-D RBC. In the turbulent regimes ($Ra \geqslant 10^8$ for $Pr = 0.1$, and $Ra > 10^9$ for $Pr = 1$), the data approximately follow $E_{av} \sim Ra^{1/3}$, shown as dashed lines. In contrast, E_{av} in 3-D RBC for $Pr = 0.7$ (taken from Samuel *et al.* 2024) shows a weakly decreasing trend. The transitions observed in this figure are related to transitions in the flow structure; see § 5.3. The statistical error bars in almost all the figures here are comparable to the thickness of the symbols. The exception is figure 6, for which the errors bars are shown explicitly.

even higher Rayleigh numbers. Fluctuations in the domain-averaged energy E follow from dynamical considerations; we will show this in § 6.

We define the average kinetic energy in the steady state, E_{av}, as

$$E_{av} = \tfrac{1}{2} u_{RMS}^2 / u_f^2, \tag{4.1}$$

where $u_{RMS} = \sqrt{\langle u_x^2 + u_z^2 \rangle_{A,t}}$ is the root mean square (RMS) velocity of the flow in the steady state, and plot it in figure 2 as a function of Ra. Before discussing differences between the two Prandtl numbers, we note the major difference between 2-D and 3-D fluctuations. In the 3-D case, for low and moderate Prandtl numbers, E_{av} is a slowly decreasing function of Ra; for example, E_{av} from a horizontally periodic cuboid of $\Gamma = 4$ for $Pr = 0.7$ (from Samuel *et al.* 2024), shown as green squares in figure 2, follows a $Ra^{-0.07}$ scaling. The corresponding behaviour for 2-D cases is that the fluctuations increase with Ra. The behaviour is different for different Pr when the Rayleigh numbers are low, but follows an approximately $Ra^{1/3}$ scaling at high Rayleigh numbers, as indicated by the blue and red dashed lines in figure 2. (Our objective is not a detailed study of differences between 2-D and 3-D convection. Some such differences have been pointed out e.g. by van der Poel *et al.* (2013) and Pandey *et al.* (2016)). The challenges posed by this increasing trend will be discussed below.

It is useful to study the variation of t_{trns} (which is the time required for E to attain some stipulated fraction of E_{av}) with respect to Ra and Pr by some simple scheme. To this end, we plot the evolution of E for $Ra = 3 \times 10^9$ and 10^{10} for $Pr = 0.1$ in figure 3. The growth of E for both Ra values is comparable for initial times but the curve for higher Ra continues to grow for a longer period before a nominally steady state is reached, but with conspicuous fluctuations.

Figure 3 suggests that $E(t)$ can be fitted with an equation of the form

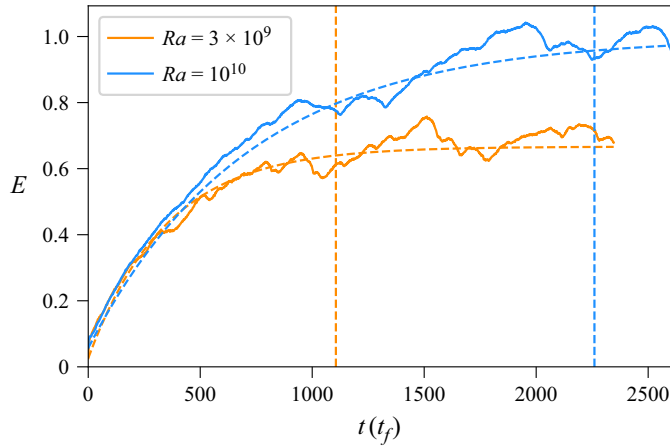$$[E_{av} - E(t)]/E_{av} = c \exp(-kt), \tag{4.2}$$

Figure 3. Evolution of the domain-averaged kinetic energy $E(t)$ in the transient state for $Pr = 0.1$ and $Ra = 3 \times 10^9$ and 10^{10} can be described well by (4.2), and the dashed curves show $E_{fit}(t)$ for the growth rate. Vertical lines show that the transient time t_{trns} is much longer for $Ra = 10^{10}$ than for $Ra = 3 \times 10^9$.

where E_{av} is the 'steady-state' or 'asymptotic' mean energy of the flow; the growth rate k depends on the Rayleigh and Prandtl numbers. The factor c captures the finite energy at the initial instant in figure 3: though $E(t)$ grows rapidly only when the convective motion is established, there is a finite $E(t)$ from which it starts.

We fit the suitable segment of the growth curve $E(t)$ with (4.2). The segment at late times is not suitable for fitting the formula because the kinetic energy does not attain a constant value but fluctuates strongly for long periods of time. The scaling factor c is calculated from the data as $c = (E_{av} - E(0))/E_{av}$, where $E(0)$ is the energy at $t = 0$. The dashed curves in figure 3 are fits to the data. Having determined the growth rate, we define the transient time t_{trns} as the time when the fitted curve $E_{fit}(t)$ in figure 3 reaches 96 % of its 'constant' value, E_{av}. Thus the transient time is estimated as

$$t_{trns} = \frac{1}{k} \log \frac{c}{0.04}. \tag{4.3}$$

The transient time thus estimated is plotted as a function of Ra in figure 4(a). Note that t_{trns} increases as a power law; for $Pr = 0.1$, the best fit yields $t_{trns} \sim Ra^{0.59 \pm 0.03}$, while we find $t_{trns} \sim Ra^{0.71 \pm 0.08}$ for $Pr = 1$.

We have experimented with different definitions of t_{trns} (e.g. by requiring it to reach 90 % of E_{av}), and find the same trends, though the numbers are different. The fact that the Ra exponent is non-trivial suggests an important role for the boundary layers and their relation to the large structure; those details (as well as the effect of the aspect ratio) are in need of further exploration.

Figure 4(a) further shows that for a given Ra, t_{trns} is longer for $Pr = 0.1$ than for $Pr = 1$. This is expected as u_{RMS} – consequently the Reynolds number – is higher for smaller Pr (Schumacher, Götzfried & Scheel 2015; Pandey & Verma 2016; Pandey *et al.* 2022a). In figure 4(b), we plot t_{trns} as a function of the Reynolds number Re, which is defined as

$$Re = u_{RMS} H / \nu. \tag{4.4}$$

We find that the two t_{trns} fall approximately on the same line for both Prandtl numbers, the best fit for which is nearly linear. Thus a 2-D RBC at high Ra has to be simulated for
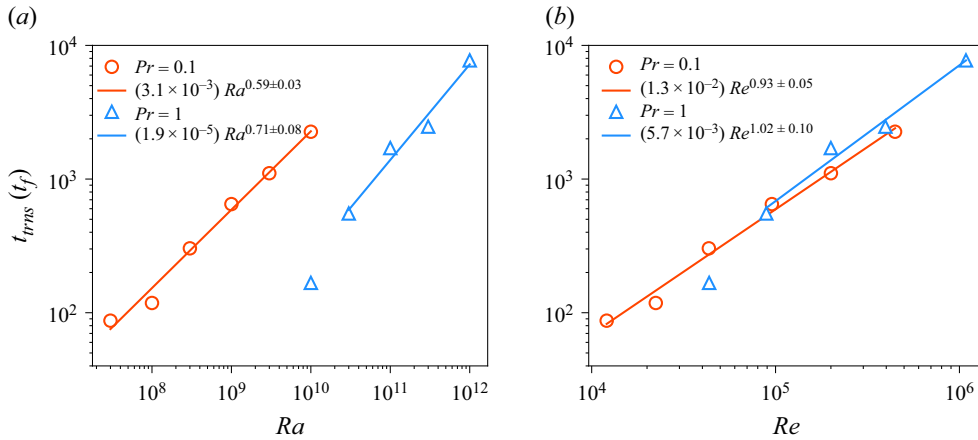
1015 A42-8

Figure 4. (*a*) The transient time t_{trns} as a function of Ra shows a power law. For a given Ra, t_{trns} is longer for lower Pr. (*b*) The time t_{trns} as a function of Re is essentially the same for both values of Pr, and exhibits a nearly linear trend. Moreover, t_{trns} is nearly the same for both Pr values when the Reynolds numbers are the same. Data correspond only to the turbulent regimes. Sparser data sets for $Pr = 0.021$ are consistent with the Prandtl numbers of these plots.
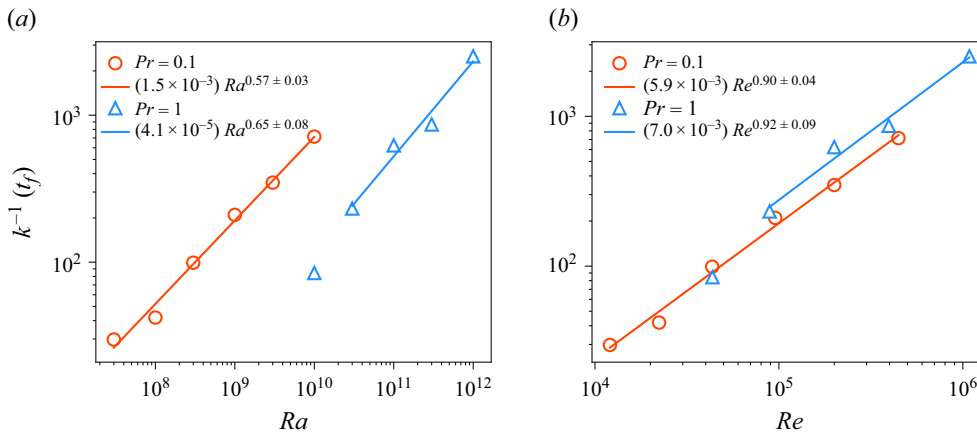
Figure 5. Inverse growth rate as a function of (*a*) Ra and (*b*) Re. The trends with Re are approximately the same for both Prandtl numbers, and are slightly below linear.

very long times to achieve a statistically steady state. If a steady state is not achieved and E is still growing, then one will find $Nu_{\varepsilon_u} < Nu$ (see § 6), even when spatial and temporal resolutions are adequate.

Shown in figure 5 is the variation of the inverse growth rate k^{-1} with respect to Ra (figure 5*a*) and Re (figure 5*b*). It appears that k^{-1} is approximately a linear function of Re, and depends only weakly on the Prandtl number.

A longer transient at higher Ra compels researchers to use some workaround to achieve the statistically steady state in a shorter time. For example, one might start with a much coarser resolution and ramp it up to the required level only after the kinetic energy has reached an approximate steady state. It is practically impossible with available computing power to conduct very high Ra simulation with fully-resolved fields in the entire transient state. One can use a coarser mesh during the transient when all degrees of freedom have not yet been excited. However, it is important to ensure that simulations on the coarser
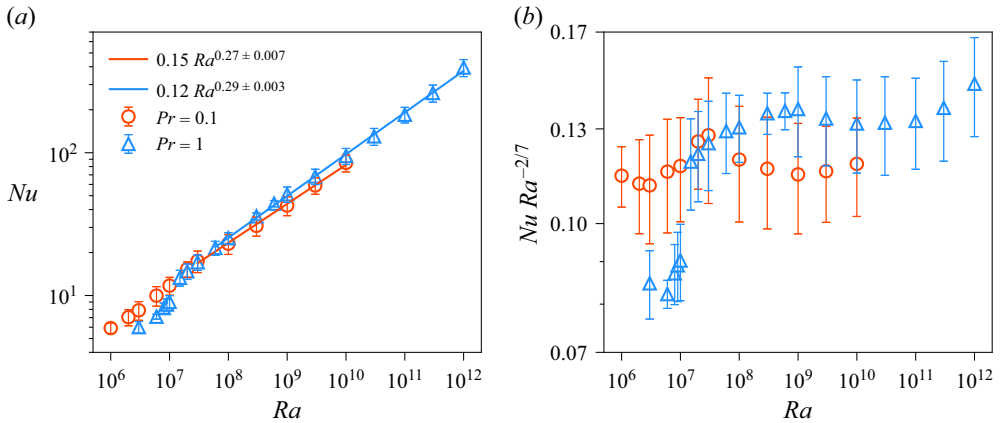
Figure 6. (*a*) The Nusselt number as a function of Ra for $Pr = 0.1$ (red circles) and $Pr = 1$ (blue triangles). The scaling for high Rayleigh numbers differs only slightly from the low-Ra behaviour. (*b*) The normalised Nusselt number $Nu\,Ra^{-2/7}$ shows that the 2/7 scaling is only approximate for moderate Rayleigh numbers and moderate aspect ratios. Wall heat flux from (3.2) is shown here with the error bars representing the standard deviation.

mesh lead to the same steady state as that attained in a well-resolved simulation. A concern otherwise would be that the coarse-grid simulation results in kinetic energy different from the properly resolved case, ultimately affecting the scaling of Re, particularly because of the presence of the low frequency modes (see § 6). Though we demonstrate in Appendix A that the mean kinetic energy in the steady state and the transient time are essentially the same in coarser simulations, it is not necessarily likely to be a general result. The data in figures 1 and 3 correspond to simulations at the coarser resolution.

5. Scaling exponents for integral transport in the steady state

5.1. *Heat transport*

We plot Nu, computed from (3.2), as a function of Ra in figure 6(*a*). The data for high Rayleigh numbers seem to closely follow similar power laws for both Pr values. For $Pr = 1$, the best fit for $Ra \geqslant 6 \times 10^7$ yields the scaling $Nu = 0.12\,Ra^{0.29 \pm 0.003}$. The exponent is close to 2/7 proposed for the so-called 'hard turbulence' in confined 3-D RBC (Castaing *et al.* 1989), also explored in various later studies (Siggia 1994; Chillà & Schumacher 2012; Johnston & Doering 2009). We plot the normalised Nusselt number $Nu\,Ra^{-2/7}$ versus Ra in figure 6(*b*), which reveals that the local exponent varies considerably and is only approximately 2/7. Furthermore, we note that the Nusselt numbers fluctuate significantly, being significantly larger when Nu is computed using (3.3). To some extent, this result indicates that the local scaling exponents obtained by fitting heat transport data over short ranges of Rayleigh numbers could lead to misleading conclusions. Figure 6(*a*) also shows that the Nusselt numbers for $Ra \leqslant 10^7$ for $Pr = 1$ do not follow the higher-Ra trend. This is a consequence of differing flow structures observed: the flow for $Ra \leqslant 10^7$ consists of two vertically stacked rolls, whereas for $Ra > 10^7$, a single-roll structure is observed. These findings suggest that the flow is less efficient in transporting heat when the double-roll state occurs, which is in line with previous observations in both two and three dimensions (Xi & Xia 2008; van der Poel, Stevens & Lohse 2011; Weiss & Ahlers 2011).

For $Ra \leqslant 3 \times 10^7$, the Nusselt numbers for $Pr = 0.1$ are higher than those for $Pr = 1$. Unlike for $Pr = 1$, the flow for $Pr = 0.1$ shows no double-roll state at lower Rayleigh
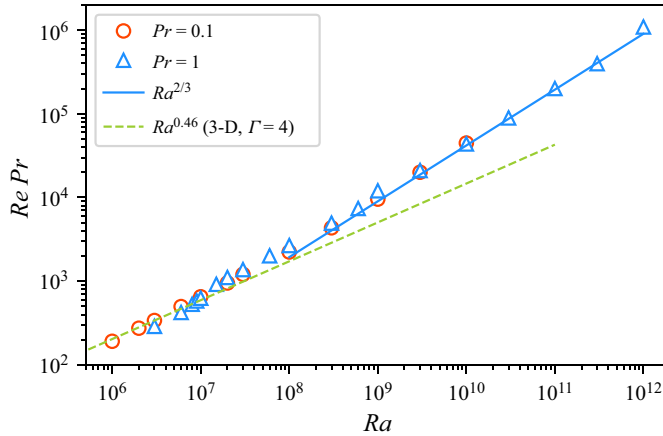
Figure 7. The Reynolds number based on u_{RMS} scales nearly as $Ra^{2/3}$ in the turbulent regime (indicated by the blue solid line), which is distinctively different from scaling $Ra^{1/2}$ reported in 3-D RBC. The green dashed line indicates the $Re \sim Ra^{0.46}$ scaling observed for 3-D RBC in a $\Gamma = 4$ box by Samuel *et al.* (2024).

numbers, which is why a larger difference appears in Nu for the two Prandtl numbers. Figure 6(*b*) clearly shows that heat transport is smaller for $Pr = 0.1$ than for $Pr = 1$ in the turbulent regime, i.e. for $Ra > 3 \times 10^7$. This feature is similar to that observed in 3-D RBC, where lower-Pr fluids are less efficient at transporting heat when $Pr < 1$ (Verzicco & Camussi 1999; van der Poel *et al.* 2013; Pandey & Sreenivasan 2021; Pandey *et al.* 2022*b*). The Grossmann–Lohse model (Grossmann & Lohse 2000, 2001) also suggests a similar trend.

5.2. *Momentum transport*

A variety of velocity scales can be defined in turbulent RBC, and can be used to define the Reynolds number Re. In cylindrical or cubic domains with $\Gamma \approx 1$, the most dominant eddy in the flow is in the form of a large-scale circulation, and its velocity is observed to scale with the free-fall velocity (Lam *et al.* 2002; Xia, Sun & Zhou 2003). In DNS, the Reynolds number is often obtained using the RMS velocity and the depth of the convective layer H (see (4.4)) (Scheel & Schumacher 2016; Pandey *et al.* 2022*b*). We plot $Re\,Pr$ against Ra in figure 7. Also indicated by the dashed line is the power law $Re\,Pr = 0.33\,Ra^{0.46}$, as found by Samuel *et al.* (2024) for $Pr = 0.7$. There is some overlap in the magnitude of the Reynolds numbers between 2-D and 3-D RBC, but the scaling exponents differ, especially for high Rayleigh numbers. In the high-Ra regime, we find that the Reynolds number scales as $Re = 0.13\,Ra^{0.65 \pm 0.01}$ for $Pr = 0.1$, and $Re = 0.02\,Ra^{0.65 \pm 0.01}$ for $Pr = 1$. The data for lower Rayleigh numbers exhibit approximately the $Re \sim Ra^{0.55}$ scaling for both Pr values.

As is well known, the Reynolds number decreases with increasing Pr in 3-D RBC (van der Poel *et al.* 2013; Pandey & Sreenivasan 2021); similarly, in 2-D RBC, the Reynolds number scales approximately as $Ra^{2/3}\,Pr^{-1}$, consistent with the result found semi-analytically by Chini & Cox (2009) and Wen *et al.* (2020). This Re scaling further suggests that

$$\frac{u_{RMS}}{u_f} = Re\,\sqrt{\frac{Pr}{Ra}} \sim Ra^{1/6}\,Pr^{-1/2}, \tag{5.1}$$
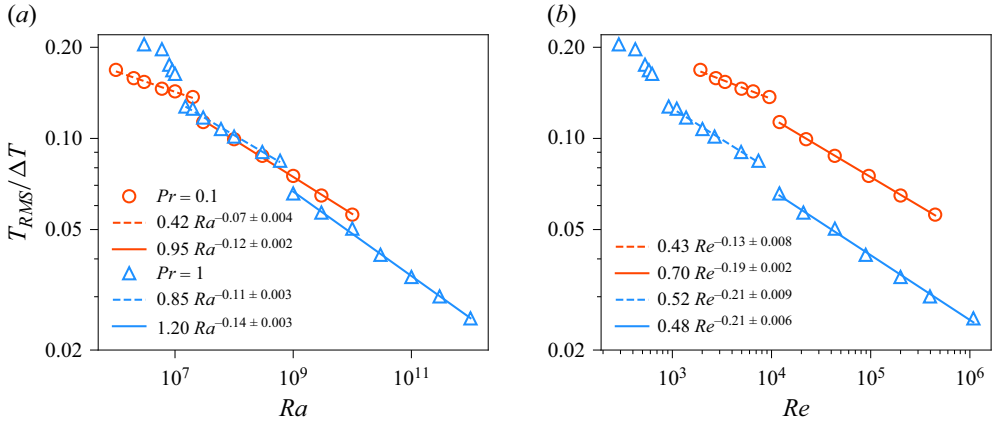
Figure 8. (*a*) The RMS temperature fluctuation T_{RMS} decreases with Ra for both Pr values, and has nearly the same magnitude for moderate Rayleigh numbers. Different exponents as well as prefactors are found for moderate and high Rayleigh numbers. (*b*) Fluctuation T_{RMS} as a function of Re shows that it scales approximately as $Re^{-0.2}$ in the turbulent regime (for $Re > 10^4$) for both Prandtl numbers.

and consequently

$$E_{av} = \frac{1}{2}\frac{u_{RMS}^2}{u_f^2} \sim Ra^{1/3}\,Pr^{-1}. \tag{5.2}$$

The high-Ra data in figure 2 are indeed consistent with this scaling.

5.3. *The RMS temperature fluctuation*

We compute the RMS temperature fluctuation as

$$T_{RMS} = \sqrt{\langle T^2 \rangle_{A,t} - \langle T \rangle_{A,t}^2}, \tag{5.3}$$

and plot $T_{RMS}/\Delta T$ as a function of Ra in figure 8(*a*). It is clear that $T_{RMS}/\Delta T$ decreases with increasing Ra, but various regions can be identified in figure 8(*a*). For $Pr = 0.1$, T_{RMS} for $Ra \leqslant 2 \times 10^7$ exhibits $Ra^{-0.07}$ scaling, but it starts, somewhat abruptly, to follow a steeper $Ra^{-0.12}$ scaling for higher Ra. For $Pr = 1$, too, we find that T_{RMS} for $Ra < 10^9$ shows a scaling $Ra^{-0.11}$, while a scaling $Ra^{-0.14}$ ensues for $Ra \geqslant 10^9$. Again, the transition between these two regimes is nearly abrupt. The RMS fluctuations for $Ra \leqslant 10^7$ are larger and clearly depart from the trend for higher Ra; this occurs because of the double-roll state observed for weak thermal forcing at $Pr = 1$. It is interesting that the scaling $Ra^{-0.14}$ for high Ra agrees well with scalings of fluctuations at the centre of cylindrical RBC cells for $Pr \approx 0.7$ (Castaing *et al.* 1989; Niemela *et al.* 2000), as well as with that in the bulk region of a horizontally periodic box for $Pr = 0.7$, $\Gamma = 4$ (Samuel *et al.* 2024); see also Pandey & Verma (2016). We also note that the magnitudes of T_{RMS} for moderate Rayleigh numbers ($10^7 < Ra < 10^9$) are quite similar for the two Prandtl numbers.

The nearly abrupt transitions in T_{RMS} are related to changes in flow morphology and statistics, and in the corresponding heat transport scaling. Data for $Pr = 0.1$ show that the scaling exponent γ in the Nu–Ra relation changes from ≈ 0.35 to ≈ 0.25 for $Ra \geqslant 3 \times 10^7$, with the latter value persisting for nearly two decades of Ra (i.e. up to $Ra \approx 10^9$), beyond which it again increases to 0.30. Similarly, for $Pr = 1$, γ changes from ≈ 0.31 to $\approx 2/7$ after the transition at $Ra \approx 10^9$. Labarre *et al.* (2023) recently noted that the ratio between

the RMS fluctuations and the mean heat flux increases abruptly in two dimensions once Ra/Pr increases beyond $\approx 10^9$. A somewhat similar transition was reported also by Gao *et al.* (2024), who found the transition Ra to scale with the Prandtl number as $Pr^{1.41}$. Our own data show that the relative fluctuations in the heat flux near the wall and in the bulk are enhanced significantly for $Ra \geqslant 3 \times 10^7$ at $Pr = 0.1$, and for $Ra \geqslant 10^9$ at $Pr = 1$ (see table 1).

The decrease in $T_{RMS}/\Delta T$ with Ra is related to the thermal boundary layer, which becomes thinner with Ra (Scheel, Kim & White 2012; Pandey 2021). As T_{RMS} represents an average measure of the temperature anomaly in the flow, the dominant contribution to T_{RMS} arises from regions occupied by thermal plumes. This is because the temperature within the plumes varies slowly and differs strongly from the ambient temperature, which is approximately the mean temperature $\Delta T/2$ in the flow. As the fraction of the volume occupied by the plumes decreases with Ra, so does their contribution to $T_{RMS}/\Delta T$. A similar magnitude of RMS fluctuations for the two Prandtl numbers (and moderate Rayleigh numbers) is due to the similar nature in the two cases of heat transport (see figure 6), which determines the thickness of the thermal boundary layer.

In figure 8(*b*), we show $T_{RMS}/\Delta T$ as a function of Re. Although the data for the two Prandtl numbers are distinct, the scaling regimes reveal themselves clearly. We observe that for large Re, the scaling exponent of $T_{RMS}/\Delta T$ with respect to Re is essentially the same for both Pr values. For $Re > 10^4$, temperature RMS exhibits the same scaling, $T_{RMS}/\Delta T \sim Re^{-0.2}$, for both Pr values. However, the exponents in moderate Reynolds numbers, to the extent that they can be defined at all, are different, with $T_{RMS}/\Delta T$ showing $Re^{-0.13}$ and $Re^{-0.21}$ for $Pr = 0.1$ and $Pr = 1$, respectively. They are unlikely to be of fundamental significance.

6. Fluctuation of global quantities

We now discuss the fluctuation of integral quantities in the nominally steady state. Taking the dot product of (2.2) with $\boldsymbol{u}$, and averaging over the entire domain, we obtain

$$\frac{\partial}{\partial t} \langle u_i^2/2 \rangle_A = \alpha g \, \langle u_z T \rangle_A - \langle \varepsilon_u \rangle_A. \tag{6.1}$$

Recalling that $E = \langle (u_x^2 + u_z^2)/2 \rangle_A / u_f^2$ is the domain-averaged kinetic energy, (6.1) takes the non-dimensional form

$$\sqrt{Ra \, Pr} \, \frac{\partial E}{\partial t} = \overline{Nu} - \overline{Nu_{\varepsilon_u}}, \tag{6.2}$$

where $\overline{Nu}$ and $\overline{Nu_{\varepsilon_u}}$ are the instantaneous domain-averaged heat fluxes defined in (3.8) and (3.9), respectively. Equation (6.2) states that $\overline{Nu}$ and $\overline{Nu_{\varepsilon_u}}$ are not equal to each other whenever E varies with time.

In figure 9, we show the temporal evolutions of $\sqrt{Ra \, Pr} \, E$, $\overline{Nu}$, $\overline{Nu_{\varepsilon_u}}$, $\overline{Nu_{\varepsilon_T}}$ in the nominally steady state for $Pr = 0.1$, $Ra = 10^{10}$. Each quantity evolves differently from the others. Figure 9(*a*) shows that domain-averaged kinetic energy E contains sizeable changes with respect to its mean value, indicated by a dashed horizontal line, occurring in 40–60 units of free-fall time. In figure 9(*c*), $\overline{Nu_{\varepsilon_u}}$ shows a slow variation superimposed by strong rapid fluctuations. In contrast, $\overline{Nu}$ in figure 9(*b*) fluctuates rapidly around its mean value. In figure 9(*d*), $\overline{Nu_{\varepsilon_T}}$ also fluctuates rapidly about its mean, with weak (but non-monotonic) trends. Data for $Ra > 10^8$ at $Pr = 0.1$ exhibit similar characteristics.
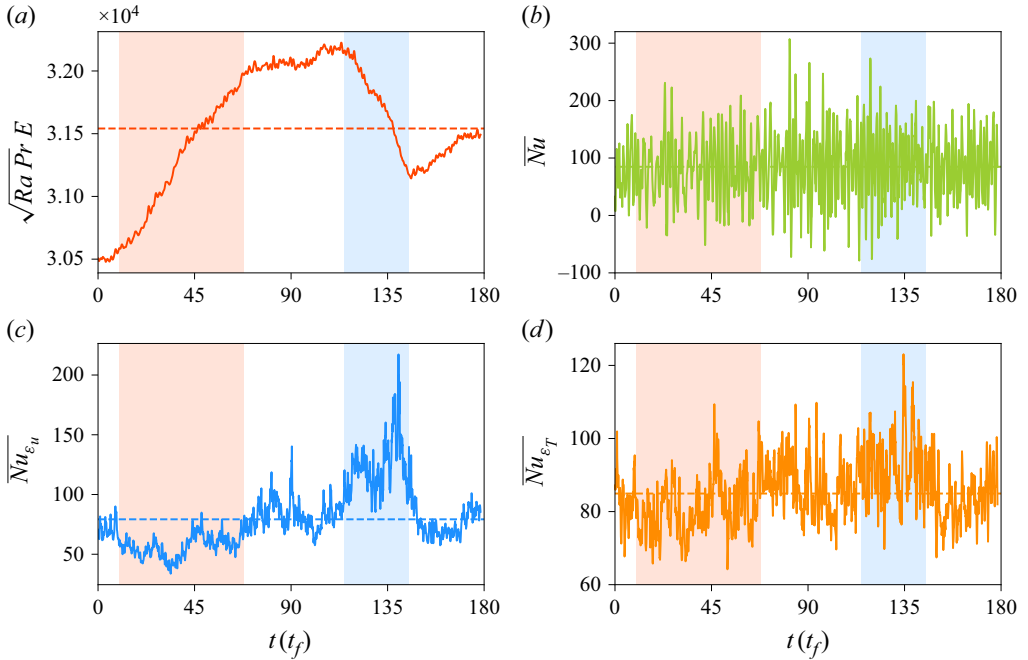
Figure 9. Temporal evolution of the integral quantities in statistically steady state for $Pr = 0.1$, $Ra = 10^{10}$: (*a*) domain-averaged scaled kinetic energy $\sqrt{Ra\,Pr}\,E$ is dominated by a slow evolution; (*b*) $\overline{Nu}$ fluctuates rapidly about its mean; (*c*) $\overline{Nu_{\varepsilon_u}}$, in addition to having rapidly fluctuating components, evolves slowly and is related to E (see (6.2)); (*d*) $\overline{Nu_{\varepsilon_T}}$ fluctuates rapidly, but a weak slowly-varying trend is present. The horizontal dashed line in all the plots indicates the time-averaged quantity. Here, the origin is taken to be $3000\,t_f$ of figure 3.

Coming to the energy balance equation, if we average (6.2) over a finite interval of time, say between an initial (non-dimensional) time t_{init} and a final time t_{fin}, then we obtain

$$\sqrt{Ra\,Pr}\,\frac{\Delta E}{\Delta t} = \langle Nu \rangle_{\Delta t} - \langle Nu_{\varepsilon_u} \rangle_{\Delta t}, \qquad (6.3)$$

where $\Delta E = E(t_{fin}) - E(t_{init})$, $\Delta t = t_{fin} - t_{init}$, and $\langle \cdot \rangle_{\Delta t}$ denotes an averaging over the time interval Δt. As there exist long periods of growth or decay of E (see figure 9*a*), we can apply (6.3) to those intervals. For example, focusing on a segment where E grows in figure 9 (the region highlighted by red shading), we find the left-hand side of (6.3) to be $\sqrt{Ra\,Pr}\,\Delta E/\Delta t = 23.8$. During this period, the average values of the heat fluxes are found to be $\langle Nu \rangle_{\Delta t} = 80.3$ and $\langle Nu_{\varepsilon_u} \rangle_{\Delta t} = 56.4$, yielding 23.9 for the right-hand side. Thus (6.3) is satisfied perfectly. Similarly, in the blue-shaded region in figure 9 where E decays, we obtain $\sqrt{Ra\,Pr}\,\Delta E/\Delta t = -33$, $\langle Nu \rangle_{\Delta t} = 90.4$ and $\langle Nu_{\varepsilon_u} \rangle_{\Delta t} = 123.5$; thus the terms of (6.3) balance perfectly again. We note that the power spectra of the quantities shown in figure 9 show slow oscillations, or low-frequency modes, in E and Nu_{ε_u}, Nu and Nu_{ε_T}, although these modes diminish in power compared to the significantly strengthening high frequencies.

On the one hand, due to the rapid fluctuation of $\overline{Nu}$ about its mean, its short-term average does not differ much from the long-term average. For example, $\langle Nu \rangle_{\Delta t} = 80.3$ and $\langle Nu \rangle_{\Delta t} = 90.4$ in the same two intervals are not far from the average 84.7. On the other hand, the presence of a strong low-frequency component in $\overline{Nu_{\varepsilon_u}}$ causes short-term averages to differ significantly from the long-term value. For example, $\langle Nu_{\varepsilon_u} \rangle_{\Delta t} = 56.4$
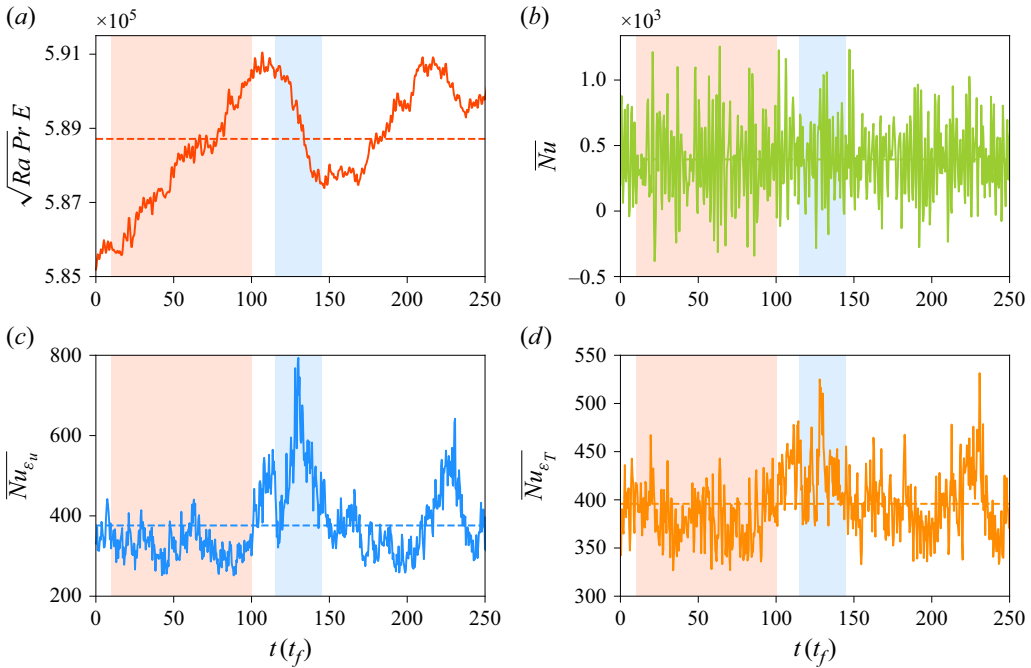
Figure 10. Temporal evolution of the integral quantities in steady state for $Pr = 1$, $Ra = 10^{12}$. The descriptions are the same as in figure 9.

and $\langle Nu_{\varepsilon_u} \rangle_{\Delta t} = 123.5$ in the growing and decaying periods of E, respectively, differ by up to 50–60 % from $Nu_{\varepsilon_u} = 79.2$. This applies to all the high-Re data in 2-D RBC that we have explored. For example, figure 10 demonstrates the same picture for $Pr = 1$, $Ra = 10^{12}$, where in the red- and blue-shaded regions, $\langle Nu \rangle_{\Delta t}$ is, respectively, larger and smaller than $\langle Nu_{\varepsilon_u} \rangle_{\Delta t}$, and (6.3) applies perfectly.

As Ra approaches very high values, the overwhelming resources required to simulate convective flows in two dimensions limit the total simulation time available to gather statistics. As a result, Nu and Nu_{ε_u} may not converge perfectly even if the sufficiency of spatial and temporal resolutions is ensured. For the simulation at $Pr = 0.1$, $Ra = 10^{10}$ (shown in figure 9), Nu and Nu_{ε_u} differ by more than 6 % (see table 1). Similarly, for $Pr = 1$, $Ra = 10^{12}$ (shown in figure 10), the difference is also approximately 5 %. For lower Ra, on the other hand, there is better convergence, to within 1–2 %. The convergence of Nu_{ε_T} and Nu is much better because both $\overline{Nu_{\varepsilon_T}}$ and $\overline{Nu}$ oscillate with comparable rapidity about their long-term averages.

7. Summary and conclusions

Our goal here has been to study the nature of the transient evolution of the DNS of 2-D thermal convection, using the no-slip boundary condition on all the walls, along with isothermal bottom and top walls, and adiabatic sidewalls. We illustrate related features using a square box for Prandtl numbers 0.1 and 1, in the Rayleigh number range between 10^6 and 10^{12}. We particularly study the temporal evolution of integral transport quantities – such as the Nusselt number (defined in three different ways) and the turbulent energy – and discuss their scaling. The nominally steady state is reached exponentially with substantial dependence on Rayleigh and Prandtl numbers. Although there is some degree of common

behaviour of transients for all the conditions explored here, there is no strict universality to the details of the exponential approach. We find, perhaps not surprisingly, that the velocity field evolves more slowly than the thermal field. That the velocity field evolves more slowly is not surprising because this evolution involves a few intermediate steps from the onset of heating changes. In the relation $Re \sim Ra^\zeta$, if the exponent $\zeta > 0.5$ as in 2-D RBC, then the ratio u_{RMS}/u_f continues to increase with Ra. It is evident from (5.2) (see also (4.2) and (4.3)) that t_{trns} increases with increasing fluctuating energy.

We also call attention to large oscillations of the velocity field in what may be regarded effectively as the steady state. One main conclusion is that these low-frequency oscillations are related to differences between the Nusselt number defined by the correlation of u_z and T, and the Nusselt number based on the energy dissipation (see (6.2)). The time to saturation of the turbulent energy is presumably dependent on the formation of the large structure (Smith & Yakhot 1993), which itself would depend on the aspect ratio. The relation between the formation of the large structure and the time to saturation remains unclear at present, but it appears that achieving the so-called ultimate state of convection for smooth boundaries is as elusive in two dimensions as in three. The naive expectation that the reduced dimensionality in two dimensions allows one to settle the question of the ultimate state by attaining high enough Ra is thwarted to some degree by the appearance of strong, low-frequency fluctuations that demand excessively long simulation times for definitive scaling relations.

Declaration of interests. The authors report no conflict of interest.

Data availability statement. The data that support the findings of this study are available from the corresponding author upon reasonable request.

Appendix A. Numerical details and effects of resolution on the transient state

As discussed in § 4, the transient time increases rapidly with Ra in 2-D RBC. Therefore, the steady state for high-Ra flows is challenging to attain because the simulations require hundreds or thousands of free-fall times in the transient state, during which the domain-averaged kinetic energy continues to increase with time. Thus in the transient flow state, conducting simulations with a mesh that resolves all relevant scales in the flow is extremely challenging due to a significant increase in the required computational resources and wait time. Therefore, we start the simulation with conduction temperature profile and random perturbations on a coarse mesh, and continue until the domain-averaged kinetic energy stops growing with time and starts to fluctuate about some mean, whose value depends on Ra and Pr. However, it is important to ensure that the steady state that is attained using a coarser mesh is close to the one that would be attained if a finer mesh is used.

To verify this, we performed simulations for a few governing parameters with different spatial resolutions, and compared the temporal evolution of the integral quantities. In
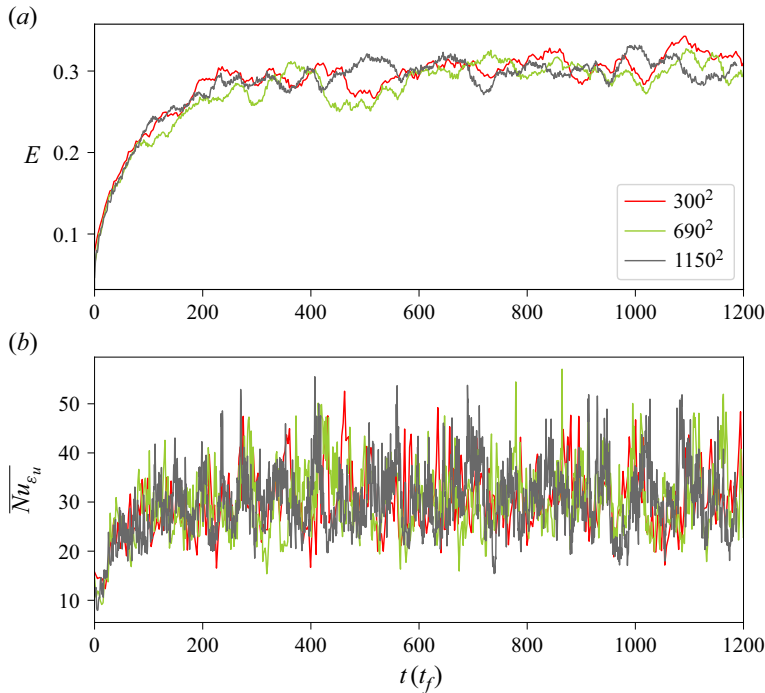
(a)

(b)

Figure 11. (a) Evolution of the domain-averaged energy E for $Pr = 0.1$, $Ra = 3 \times 10^8$ using three different spatial resolutions. The similarity of the evolutions of E, in the statistical sense, suggests that the transient time and the mean energy in the steady state do not depend on the spatial resolution. (b) Here, $\overline{Nu_{\varepsilon_u}}$ exhibits strong fluctuations, especially at moments when a rapid decay is observed in E.

figure 11(a), we show the evolution of E for $Pr = 0.1$, $Ra = 3 \times 10^8$ in three different simulations, for mesh cells of 300^2, 690^2 and 1150^2. We can see that the growth of E in the initial stage (for $t < 120\,t_f$) is similar in all simulations, although the evolutions differ slightly for intermediate stages. However, once E stops growing and starts fluctuating about some mean, the average value of energy in the steady state does not depend on the spatial resolution. We find that the mean energy for $t > 400 t_f$ in figure 11(a) differs only by at most 2 %. We also show the evolution of $\overline{Nu_{\varepsilon_u}}$ in figure 11(b) for the three simulations, and observe wild fluctuations, especially when E decreases rapidly over a short time interval. Thus the flow properties in the steady state seem to be largely unaffected by the spatial resolution used in the transient state.

Similarly, figure 12 shows E for intermediate stages of the transient state for $Pr = 1$, $Ra = 10^{12}$. We start the simulation with a coarse resolution having 690^2 mesh cells (red curve). While E is still growing, we ramp up the resolution and start another simulation with 5210^2 mesh cells (green curve), in addition to continuing the original one. Figure 12 shows that the trajectories of E in both simulations are similar, while the computational resources differ substantially. On the one hand, simulation with the coarse mesh consumes only one thousand core hours, and the segment shown in figure 12 was obtained in just eight hours on 128 cores. On the other hand, simulation with the finer mesh takes more than 900 hours on 1024 cores (green curve). As the transient time is nearly $8000\,t_f$ for these parameters (see figure 4), one would need to run the simulation with 5210^2 mesh cells for 72 000 h on 1024 cores to attain the steady state, which is clearly impossible at present.
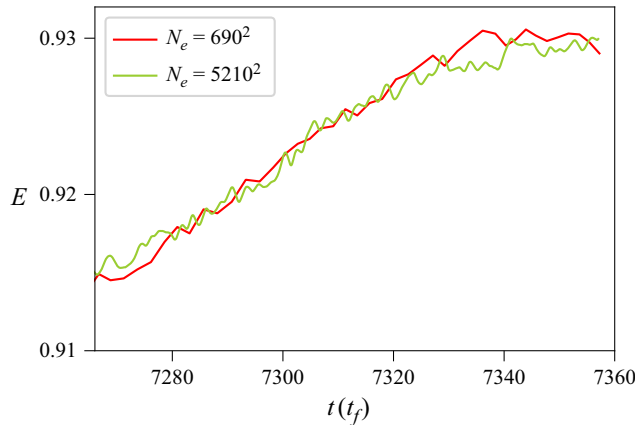
Figure 12. Evolution of the kinetic energy in the intermediate stage of the transient state for $Pr = 1$, $Ra = 10^{12}$. Computational time is close to one million core-hours for the simulation with 5210^2 mesh cells – much bigger than one thousand core hours needed for simulation with 690^2 cells. It is clear that performing high-Ra simulation in the transient state with full resolution is infeasible.

REFERENCES

CASTAING, B., GUNARATNE, G., KADANOFF, L., LIBCHABER, A. & HESLOT, F. 1989 Scaling of hard thermal turbulence in Rayleigh–Bénard convection. *J. Fluid Mech.* **204**, 1–30.

CHILLÀ, F. & SCHUMACHER, J. 2012 New perspectives in turbulent Rayleigh–Bénard convection. *Eur. Phys. J. E* **35** (7), 58.

CHINI, G.P. & COX, S.M. 2009 Large Rayleigh number thermal convection: heat flux predictions and strongly nonlinear solutions. *Phys. Fluids* **21** (8), 083603.

DOERING, C.R. 2020 Absence of evidence for the ultimate state of turbulent Rayleigh–Bénard convection. *Phys. Rev. Lett.* **124** (22), 229401.

DOERING, C.R., TOPPALADODDI, S. & WETTLAUFER, J.S. 2019 Absence of evidence for the ultimate regime in two-dimensional Rayleigh–Bénard convection. *Phys. Rev. Lett.* **123** (25), 259401.

FOROOZANI, N., NIEMELA, J.J., ARMENIO, V. & SREENIVASAN, K.R. 2014 Influence of container shape on scaling of turbulent fluctuations in convection. *Phys. Rev. E* **90** (6), 063003.

FOROOZANI, N., NIEMELA, J.J., ARMENIO, V. & SREENIVASAN, K.R. 2017 Reorientations of the large-scale flow in turbulent convection in a cube. *Phys. Rev. E* **95** (3), 033107.

GAO, Z.-Y., TAO, X., HUANG, S.-D., BAO, Y. & XIE, Y.-C. 2024 Flow state transition induced by emergence of orbiting satellite eddies in two-dimensional turbulent Rayleigh–Bénard convection. *J. Fluid Mech.* **997**, A54.

GROSSMANN, S. & LOHSE, D. 2000 Scaling in thermal convection: a unifying theory. *J. Fluid Mech.* **407**, 27–56.

GROSSMANN, S. & LOHSE, D. 2001 Thermal convection for large Prandtl numbers. *Phys. Rev. Lett.* **86** (15), 3316–3319.

HOWARD, L.N. 1972 Bounds on flow quantities. *Annu. Rev. Fluid Mech.* **4** (1), 473–494.

IYER, K.P., SCHEEL, J.D., SCHUMACHER, J. & SREENIVASAN, K.R. 2020 Classical 1/3 scaling of convection holds up to $Ra = 10^{15}$. *Proc. Natl Acad. Sci. USA* **117** (14), 7594–7598.

JOHNSTON, H. & DOERING, C.R. 2009 Comparison of turbulent thermal convection between conditions of constant temperature and constant flux. *Phys. Rev. Lett.* **102** (6), 064501.

KADANOFF, L.P. 2001 Turbulent heat flow: structures and scaling. *Phys. Today* **54** (8), 34–39.

LABARRE, V., FAUVE, S. & CHIBBARO, S. 2023 Heat-flux fluctuations revealing regime transitions in Rayleigh–Bénard convection. *Phys. Rev. Fluids* **8** (5), 053501.

LAM, S., SHANG, X.-D., ZHOU, S.-Q. & XIA, K.-Q. 2002 Prandtl number dependence of the viscous boundary layer and the Reynolds numbers in Rayleigh–Bénard convection. *Phys. Rev. E* **65** (6), 066306.

LOHSE, D. & SHISHKINA, O. 2023 Ultimate turbulent thermal convection. *Phys. Today* **76** (11), 26–32.

LOHSE, D. & SHISHKINA, O. 2024 Ultimate Rayleigh–Bénard turbulence. *Rev. Mod. Phys.* **96** (3), 035001.

NIEMELA, J.J., SKRBEK, L., SREENIVASAN, K.R. & DONNELLY, R.J. 2000 Turbulent convection at very high Rayleigh numbers. *Nature* **404** (6780), 837–840.

PANDEY, A. 2021 Thermal boundary layer structure in low-Prandtl-number turbulent convection. *J. Fluid Mech.* **910**, A13.

PANDEY, A., KRASNOV, D., SCHUMACHER, J., SAMTANEY, R. & SREENIVASAN, K.R. 2022*a* Similarities between characteristics of convective turbulence in confined and extended domains. *Physica D* **442**, 133537.

PANDEY, A., KRASNOV, D., SREENIVASAN, K.R. & SCHUMACHER, J. 2022*b* Convective mesoscale turbulence at very low Prandtl numbers. *J. Fluid Mech.* **948**, A23.

PANDEY, A., KUMAR, A., CHATTERJEE, A.G. & VERMA, M.K. 2016 Dynamics of large-scale quantities in Rayleigh–Bénard convection. *Phys. Rev. E* **94** (5), 053106.

PANDEY, A. & SREENIVASAN, K.R. 2021 Convective heat transport in slender cells is close to that in wider cells at high Rayleigh and Prandtl numbers. *Europhys. Lett.* **135** (2), 24001.

PANDEY, A. & VERMA, M.K. 2016*a* Scaling of large-scale quantities in Rayleigh–Bénard convection. *Phys. Fluids* **28** (9), 095105.

PANDEY, A., VERMA, M.K., CHATTERJEE, A.G. & DUTTA, B. 2016*b* Similarities between 2D and 3D convection for large Prandtl number. *Pramana – J. Phys.* **87** (1), 13.

VAN DER POEL, E.P., STEVENS, R.J.A.M. & LOHSE, D. 2011 Connecting flow structures and heat flux in turbulent Rayleigh–Bénard convection. *Phys. Rev. E* **84** (4), 045303(R).

VAN DER POEL, E.P., STEVENS, R.J.A.M. & LOHSE, D. 2013 Comparison between two- and three-dimensional Rayleigh–Bénard convection. *J. Fluid Mech.* **736**, 177–194.

SAMUEL, R. & VERMA, M.K. 2024 Bolgiano–Obukhov scaling in two-dimensional Rayleigh–Bénard convection at extreme Rayleigh numbers. *Phys. Rev. Fluids* **9** (2), 023502.

SAMUEL, R.J., BODE, M., SCHEEL, J.D., SREENIVASAN, K.R. & SCHUMACHER, J. 2024 No sustained mean velocity in the boundary region of plane thermal convection. *J. Fluid Mech.* **996**, A49.

SCHEEL, J.D., EMRAN, M.S. & SCHUMACHER, J. 2013 Resolving the fine-scale structure in turbulent Rayleigh–Bénard convection. *New J. Phys.* **15** (11), 113063.

SCHEEL, J.D., KIM, E. & WHITE, K.R. 2012 Thermal and viscous boundary layers in turbulent Rayleigh–Bénard convection. *J. Fluid Mech.* **711**, 281–305.

SCHEEL, J.D. & SCHUMACHER, J. 2016 Global and local statistics in turbulent convection at low Prandtl numbers. *J. Fluid Mech.* **802**, 147–173.

SCHMALZL, J., BREUER, M. & HANSEN, U. 2004 On the validity of two-dimensional numerical approaches to time-dependent thermal convection. *Europhys. Lett.* **67** (3), 390–396.

SCHUMACHER, J., GÖTZFRIED, P. & SCHEEL, J.D. 2015 Enhanced enstrophy generation for turbulent convection in low-Prandtl-number fluids. *Proc. Natl Acad. Sci. USA* **112** (31), 9530–9535.

SCHUMACHER, J. & SREENIVASAN, K.R. 2020 Colloquium: unusual dynamics of convection in the Sun. *Rev. Mod. Phys.* **92** (4), 041001.

SHRAIMAN, B.I. & SIGGIA, E.D. 1990 Heat transport in high-Rayleigh-number convection. *Phys. Rev. A* **42** (6), 3650–3653.

SIGGIA, E.D. 1994 High Rayleigh number convection. *Annu. Rev. Fluid Mech.* **26** (1), 137–168.

SMITH, L.M. & YAKHOT, V. 1993 Bose condensation and small-scale structure generation in a random force driven 2D turbulence. *Phys. Rev. Lett.* **71** (3), 352–355.

SREENIVASAN, K.R., BERSHADSKII, A. & NIEMELA, J.J. 2002 Mean wind and its reversal in thermal convection. *Phys. Rev. E* **65** (5), 056306.

STEVENS, R., LOHSE, D. & VERZICCO, R. 2011 Prandtl and Rayleigh number dependence of heat transport in high Rayleigh number thermal convection. *J. Fluid Mech.* **688**, 31–43.

STEVENS, R., VERZICCO, R. & LOHSE, D. 2010 Radial boundary layer structure and Nusselt number in Rayleigh–Bénard convection. *J. Fluid Mech.* **643**, 495–507.

STEVENS, R.J., HARTMANN, R., VERZICCO, R. & LOHSE, D. 2024 How wide must Rayleigh–Bénard cells be to prevent finite aspect ratio effects in turbulent flow? *J. Fluid Mech.* **1000**, A58.

TIWARI, H., SHARMA, L. & VERMA, M.K. 2025 Compressible turbulent convection at very high Rayleigh numbers. *Intl J. Heat Mass Transfer* **242**, 126821.

VERMA, M.K. 2018 *Physics of Buoyant Flows*. World Scientific.

VERMA, M.K., KUMAR, A. & PANDEY, A. 2017 Phenomenology of buoyancy-driven turbulence: recent results. *New J. Phys.* **19** (2), 025012.

VERZICCO, R. & CAMUSSI, R. 1999 Prandtl number effects in convective turbulence. *J. Fluid Mech.* **383**, 55–73.

WAN, Z.-H., WANG, Q., WANG, B., XIA, S.-N., ZHOU, Q. & SUN, D.-J. 2020 On non-Oberbeck–Boussinesq effects in Rayleigh–Bénard convection of air for large temperature differences. *J. Fluid Mech.* **889**, A10.

WEISS, S. & AHLERS, G. 2011 Turbulent Rayleigh–Bénard convection in a cylindrical container with aspect ratio $\gamma = 0.50$ and Prandtl number $Pr = 4.38$. *J. Fluid Mech.* **676**, 5–40.

WEN, B., GOLUSKIN, D., LEDUC, M., CHINI, G.P. & DOERING, C.R. 2020 Steady Rayleigh–Bénard convection between stress-free boundaries. *J. Fluid Mech.* **905**, R4.

XI, H. & XIA, K. 2008 Flow mode transitions in turbulent thermal convection. *Phys. Fluids* **20** (5), 5104.

XIA, K.Q., SUN, C. & ZHOU, S.Q. 2003 Particle image velocimetry measurement of the velocity field in turbulent thermal convection. *Phys. Rev. E* **68** (6), 066303.

ZHANG, Y., ZHOU, Q. & SUN, C. 2017 Statistics of kinetic and thermal energy dissipation rates in two-dimensional turbulent Rayleigh–Bénard convection. *J. Fluid Mech.* **814**, 165–184.

ZHU, X., MATHAI, V., STEVENS, R.J.A.M., VERZICCO, R. & LOHSE, D. 2018 Transition to the ultimate regime in two-dimensional Rayleigh–Bénard convection. *Phys. Rev. Lett.* **120** (14), 144502.